








Unstable oscillatory flow of non-Brownian suspensions in Hele-Shaw cellsA. A. Garcia ^{1,2,*}, Y. L. Roht ^{1,†}, G. Gauthier ², D. Salin ², G. Drazer ³,
J. P. Hulin ² and I. Ippolito ¹¹*Universidad de Buenos Aires, Facultad de Ingeniería, Grupo de Medios Porosos,
Paseo Colón 850, 1063, Buenos Aires, Argentina*²*Université Paris-Saclay, CNRS, FAST, 91405 Orsay, France*³*Mechanical and Aerospace Engineering Department, Rutgers, The State University of New Jersey,
Piscataway, New Jersey 08854, USA*

(Received 2 August 2022; accepted 13 February 2023; published 10 March 2023)

The behavior of neutrally buoyant, non-Brownian suspensions subject to square-wave flow oscillations in Hele-Shaw cells is investigated. The velocity field across the cell gap is determined by tracking particles in a plane parallel to the main flow. Initially, the velocity field of the particles is parallel to the main flow and its profile across the gap is blunted due to a higher volume fraction of particles in the gap center; this has been confirmed by direct estimations of the particle fraction and likely results from shear-induced migration. Velocity fluctuations, both along and transverse to the flow direction, agree reasonably well with previous studies. At longer times, the suspension develops an instability characterized by the growth of a transverse velocity component that is periodic along the main flow direction and in time. No influence of inertia on the characteristic onset time of this instability is observed for Reynolds numbers varying over four decades below $Re = 0.4$. The inverse of the onset time increases linearly with the amplitude of the oscillatory flow. The dependence of the onset time on the particle volume fraction and the gap thickness is consistent with the characteristic time for particle migration across the gap due to shear-induced diffusion.

DOI: [10.1103/PhysRevFluids.8.034301](https://doi.org/10.1103/PhysRevFluids.8.034301)**I. INTRODUCTION**

Suspensions of non-Brownian particles in viscous fluids are present both in industrial (waste treatment, slurries, transport of pastes or granulates), and natural (coastal dynamics, landslides, dispersion of pollutants, siltation) flows. During the last two decades, studies of suspensions were performed both at the micro- and macro-scales [1]. In particular, the rheology of macroscopic suspensions and the crucial role of particle contacts has been highlighted in both steady [2,3] and unsteady [4] flows. In the case of macroscopic suspensions at low Reynolds numbers, these contacts result in a particle contribution to pressure [5–8] and to normal stress differences [9,10]. From a microscopic point of view, the particle roughness and the collisions between particles can result in their diffusive motion [11–14]. Both approaches (diffusive motion and particle pressure) have been used successfully to explain the so-called shear-induced migration of particles from regions of high to low shear rate of the flow [15–17]; however, at a macroscopic level, the lack of migration in certain geometries could only be explained from the normal stress differences [5].

In pressure-driven flows of suspensions through cylindrical tubes and channels with large aspect ratio, normal stresses induce migration of the particles towards the tube axis and the gap center,

*aagarcia@fi.uba.ar

†yroht@fi.uba.ar

respectively, in both steady [17,18] and oscillatory [19] flows. For noncircular ducts, like channels with square and rectangular cross sections, secondary flows occur due to normal stress differences [20–22]. There is still shear-induced migration but the spatial distribution of particles may be changed by the secondary flows. A macrotransport approach was also used recently to describe suspension flows inside a Hele-Shaw cell [23]. They considered the limit of fast migration and suggested that volume fraction gradients in the flow direction could also generate secondary flows which might influence the flow stability. In any case, in order to investigate the asymptotic distribution of particles in the cross section, exceedingly long systems would be required [24]. Thus, some authors have instead studied long time variations of the particle distribution in oscillatory flows [19], which produce large cumulative deformations of the suspension without requiring very long channels. However, upon shear reversal, a transient reduction in suspension viscosity is observed, possibly due to changes in particle microstructure and temporary loss of contacts [4,25]. Moreover, for small enough oscillation displacements, the system of particles reaches a so-called absorbing state, where they no longer collide and there is no change in the system from one period to the next [26,27]. Therefore, oscillatory flow may show additional features compared with steady flow along long channels.

In a previous work [28], we reported an instability occurring when a neutrally buoyant suspension of non-Brownian particles is subject to an oscillatory flow in a rectangular cell with large aspect ratio (Hele-Shaw cell). After the instability develops, light transmission through the cell aperture displays a two-dimensional periodic array of stripes perpendicular to the mean flow and following the oscillatory motion of the fluid. The measured wavelength of the stripes increases with the oscillation amplitude but is independent of the oscillation period for a given amplitude. The onset time for the instability depends on the particle concentration and oscillation amplitude. This instability is different from previously reported ones in suspensions with non-neutrally buoyant particles [29], with Brownian particles [30,31], for inertial flows [32], and for shear-thickening suspensions near the jamming transition [33].

In the present study, using the same particle size and flow geometry as in Ref. [28], we determine the particle velocity field both in the initial state and during the development of the instability. This is achieved by using particles with the same optical index and density as the liquid, providing a transparent dispersion of neutrally buoyant particles. The motion of a small fraction of the particles tagged by a fluorescent dye is tracked in order to determine particle velocity components parallel and perpendicular to the mean flow and to estimate particle volume fraction profiles.

After describing the experimental setup and suspensions used in this work, we discuss measurements of the mean profile and fluctuations of the velocity of the particles before the onset of the instability. We discuss then the influence of the instability on the particle trajectories and the occurrence of a transverse velocity component periodic in time and space. Finally, we define a characteristic time for the growth of the instability from the autocorrelation of the transverse velocity; its dependence on the oscillation amplitude of the flow and the volume fraction is discussed and compared with that of the characteristic time for shear-induced migration.

II. EXPERIMENTAL PROCEDURE, MATERIALS, AND DATA PROCESSING

A. Experimental setup and suspension preparation

We use a suspension of poly(methyl methacrylate) (PMMA) spheres in an aqueous solution with the following typical composition: 39.4% in weight (wt) of ammonium thiocyanate (NH_4SCN), 36.7 %wt of glycerin, and 23.9 %wt of water [34,35]. At room temperature (21 °C), the solution has the same optical index ($n = 1.49$) and density ($\rho_0 = 1.19 \text{ g/cm}^3$) as PMMA and a viscosity $\mu_0 = 7.6 \text{ mPa s}$ (as measured by an Anton Paar MCR501 rheometer). The spheres (CA40 Spheromers provided by Microbeads AS) have a diameter $d = 40 \pm 2 \text{ }\mu\text{m}$ (as measured with a Malvern Morpho G2 apparatus). To track their motion by laser-induced fluorescence, a small fraction of the spheres ($\approx 1\%$) is dyed by immersion in a solution of ethanol and rhodamine at 40 °C and dried before they

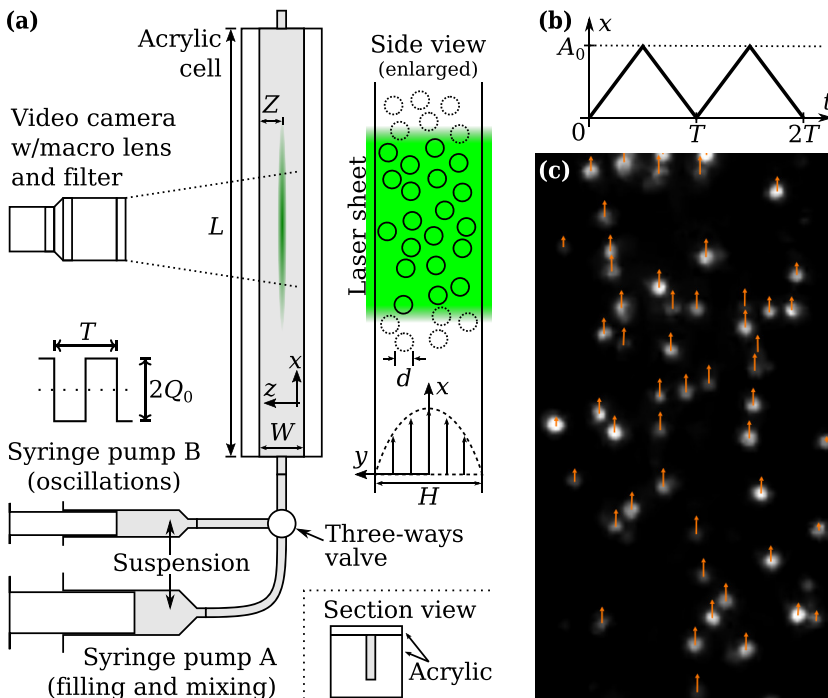


FIG. 1. (a) Schematic view of the experimental setup. Cell dimensions: $H=1\pm 0.05$ mm, $W=11\pm 0.5$ mm, $L=200$ mm. (b) Schematic variation of fluid displacement induced by the square-wave flow oscillations. (c) Small region ($1 \text{ mm} \times 2 \text{ mm}$) of a snapshot of the fluorescent particles. The arrows indicate the computed velocities of the tracked particles.

are mixed with the other beads [36]. As a result, the dyed particles shine in orange when illuminated by green light (wavelength $\lambda = 532$ nm). The volume fraction ϕ of the particles ranges between 20% and 40%. Suspensions with $\phi = 20\%$ are first prepared and the composition of the solution is fine tuned to optimize transparency and density. Solutions with higher particle volume fractions are obtained by adding particles to this first one.

In addition, two other suspending fluids were prepared and used in a limited number of experiments. First, a solution composed of Triton-X 100 (73.9 %wt), ZnCl_2 (14.2 %wt), and water (11.9 %wt) which has a much higher viscosity ($\mu_0 = 3$ Pa s according to Ref. [37]). Second, an aqueous solution of glycerin (71.8 %wt) that matches the density, but not the refractive index of the particles, allowing the qualitative observation of variations in particle distribution along the length and width of the cell.

The experimental setup is shown in Fig. 1(a). The suspension oscillates inside a rectangular slot machined inside a PMMA block and closed thereafter by a PMMA plate. Two cells were constructed in this way: one of gap thickness $H = 1$ mm and another with $H = 2$ mm. All the experiments presented here used the first one unless otherwise stated. The corresponding gap/sphere size ratios H/d are 25 and 50. The slot length L is kept vertical so that the cell may be filled up and drained more easily without trapping air. Some experiments were performed with the cell placed horizontally (gravity in the gap direction) and provided similar results.

A 25 cm^3 syringe filled with the suspension is attached to a pump [pump A in Fig. 1(a)] and the suspension is injected slowly into the setup to saturate the connecting tubes and valves. The flow rate is kept low in order to allow for the evacuation of residual air bubbles by gravity. The injection is stopped when the suspension reaches the top of the experimental cell. After the complete saturation of the cell by the suspension and the evacuation of any residual air, we switch to a different pump

[pump B in Fig. 1(a)]. It uses a smaller syringe (1 cm³), also filled with the suspension, which enables a more precise control of the oscillating flow.

We use the small syringe to create symmetric square-wave flow oscillations with a period ranging from $T = 2$ to 20 s. The typical absolute volume flow rate is $Q_0 = 13.3$ mm³/s, leading to a superficial velocity $V_0 = Q_0/S \simeq 1.16$ mm/s, where $S = 11.5$ mm² is the average area of the cross section, measured by filling the cell in a vertical position with water and monitoring the ascension of the liquid-air interface. The mean amplitude $A_0 = V_0 T/2$ of the displacement of the suspension during a half period ranges between 1.3 and 11.6 mm and is shown schematically in Fig. 1(b). For this flow rate and the fluid used in most experiments, the Reynolds number of the suspension is then $Re = V_0 H \rho_0 / \mu_0 \simeq 0.2$.

To investigate the dependence of the results on the flow rate, additional experiments were performed for Q_0 between 3.3 and 53.3 mm³/s. In addition, to validate the absence of inertial effects, experiments with a Triton-based suspending fluid of larger viscosity (3 Pa s) and with $Q_0 = 1$ mm³/s were performed. Overall, we explored a range of Re values between 4×10^{-5} and 0.4.

B. Image analysis and particle velocity determination

A laser sheet (green, $\lambda = 532$ nm) parallel to the (x, y) plane illuminates the flow channel [see Fig. 1(a)]. This orientation of the light sheet was selected based on our previous experiments which suggest that the flow created by the instability is two dimensional and contained in the (x, y) plane. The distance of the light sheet from the side wall through which observations are performed is generally $\simeq 3$ mm; however, several experiments were performed at 5 mm ($\simeq W/2$) without excessive light absorption and gave similar results. An optical notch filter eliminates the direct green illumination so that only the orange fluorescence light is detected. A digital camera provides images of the moving particles with a field of view of 1×22 mm² and frame rates up to 200 fps. A typical image is shown in Fig. 1(c).

Once acquired, the images are enhanced by convoluting them with a circle of the same radius as the experimental particles. Following this process, only the images of the beads are clearly visible. Residual low-intensity noise is eliminated using a threshold intensity and the positions of the particle centers are determined from the local maxima of the light intensity. Finally, the positions of the particles in consecutive images are compared and those spaced by less than one or two particle radii are joined into trajectories (the frame rate is adjusted so that this spacing remains small enough). The instantaneous velocity components v_x and v_y are computed for each particle from the displacement between two frames and averaged spatially and/or in time depending on the information of interest.

III. VELOCITY FIELD AND VOLUME FRACTION IN THE INITIAL STATE

This section discusses profiles of the velocity components and their fluctuations and of the particle volume fraction, in the initial part of the experiments before the instability has occurred.

A. Longitudinal velocity profile

The transverse profile of the mean longitudinal velocity is computed by first dividing the gap H into bins of width $\Delta y = H/n$ ($n = 128$); the x component v_x of the velocity of the particles inside each bin is then averaged to obtain an instantaneous mean velocity profile $V_x(y, t)$. Lower case letters are used for velocity components of individual particles, capital letters for averages. When needed, a time-averaged profile $\overline{|V_x|}(y)$ is obtained by averaging the absolute value $|V_x|(y, t)$ over the four or five first periods T when the instability is not yet present; in each period, only time lapses during which $|V_x|(y, t)$ is approximately constant [indicated in red in Fig. 2(a)] are included. The reference value $\overline{V_x}$ of the longitudinal velocity is taken to be the average of $\overline{|V_x|}(y)$ over y . Moreover, the average over y of the instantaneous velocity profiles $V_x(y, t)$ is referred to as $\overline{V_x}(t)$ and changes sign with the main flow (the longitudinal oscillations imposed by the pump).

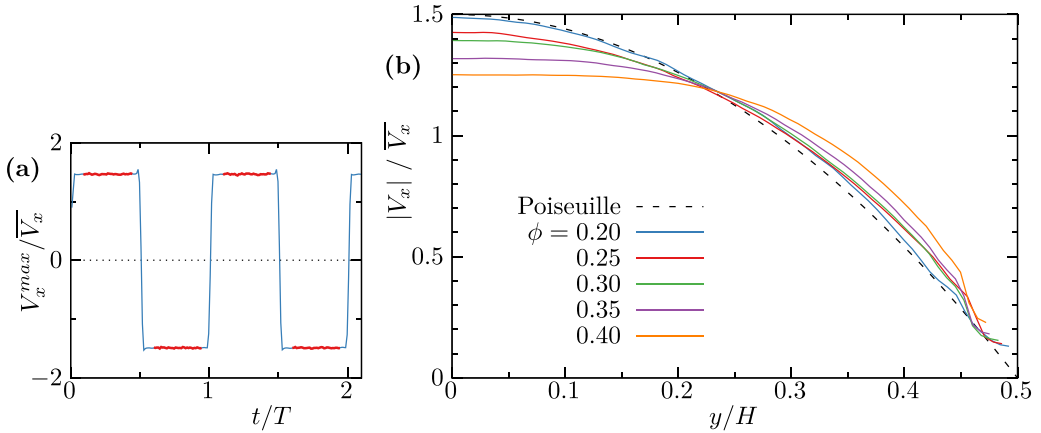


FIG. 2. (a) Experimental time variation of the maximum velocity $V_x^{\max}(t)$ at $y/H = 0$ for a very dilute suspension ($\phi < 1\%$) and $A_0/H = 4.6$. The red parts of the curve indicate time intervals with stationary flow. (b) Transverse (half) profiles of $|V_x|(y)/\bar{V}_x$. Same flow parameters as in panel (a), but ϕ ranges from 20% to 40%. Dashed line shows parabolic Poiseuille profile.

For dilute suspensions, the value of \bar{V}_x deduced from particle velocity measurements agrees with the superficial velocity V_0 . For high volume fractions ($\phi \gtrsim 20\%$) however, we observe discrepancies between these two values, together with a large dispersion in the measured \bar{V}_x . For $\phi = 40\%$, there is a $\approx 20\%$ difference between the maximum and minimum measured values of \bar{V}_x . This may be due to random variations of the distribution of the particles at the beginning of each experiment. Such variations may induce inhomogeneities in the volume fraction and longitudinal flow velocity across the width W . Therefore, in order to compare results from different experiments, we normalize all velocities by the reference value \bar{V}_x determined experimentally. Normalized velocity profiles $|V_x|(y)/\bar{V}_x$ are shown in Fig. 2(b) for different volume fractions.

At the lowest volume fraction [$\phi = 20\%$, blue line in Fig. 2(b)], the experimental velocity profile at early times is close to a Poiseuille profile [dashed line in Fig. 2(b)]: the ratio $|V_x|(y)/\bar{V}_x$ is then approximately 1.5 at the center of the gap ($y = 0$). As ϕ increases from 20% to 40%, the profiles becomes more blunted, in agreement with previous work on shear-induced migration [18,19,24,38]. Figure 3 compares normalized velocity profiles obtained for two mean volumes fractions to results

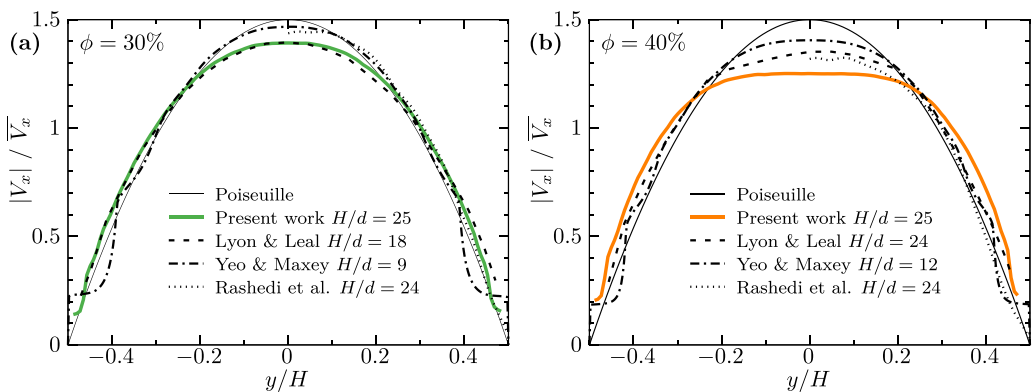


FIG. 3. Longitudinal velocity profiles across the gap compared with experimental and numerical results from the literature for two mean particle volume fractions, $\phi = 30\%$ and 40% (same experiments as in Fig. 2).

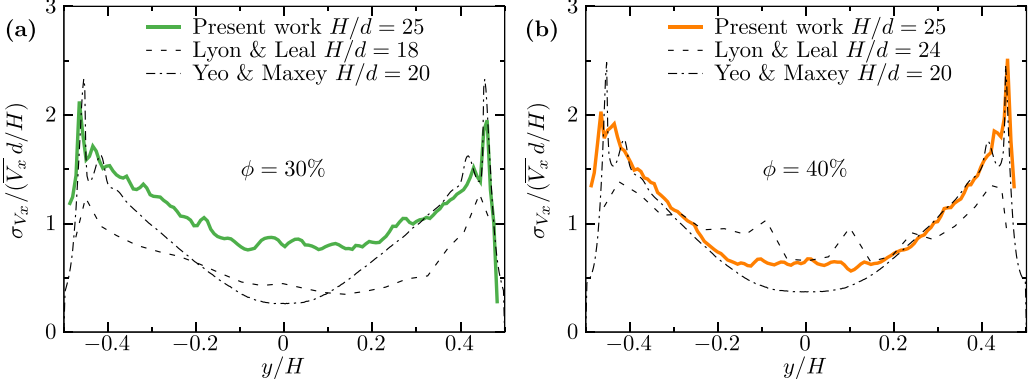


FIG. 4. Normalized longitudinal velocity fluctuations across the gap compared with experimental and numerical results from the literature. Same experiments as in Fig. 3.

from previous studies [18,24,38]. Although all previous studies considered here share the same trend as our results, with more blunted profiles at higher volume fractions, the quantitative values display some dispersion. The observed discrepancies could originate in the use of different methods to prepare the suspensions and start the flow, or may be due to differences in the normalization of the curves. The same considerations apply to comparisons discussed in later sections.

B. Longitudinal velocity fluctuations

In addition to the average velocity, we compute the root mean square (rms) $\sigma_{v_x}(y, t) = [v_x^2 - V_x^2(y, t)]^{1/2}$ of the velocity fluctuations. Then, we compute its time average $\sigma_{V_x}(y)$ over the same set of time intervals used to obtain $|V_x|(y)$. Since the velocity fluctuations are expected to be proportional to the shear rate ($\sim \overline{V_x}/H$) and to the particle diameter (d) [17], we present in Fig. 4 the profile of the fluctuations $\sigma_{V_x}(y)$ normalized by $\overline{V_x}d/H$. The fluctuations are smaller at the center of the gap and reach a maximum at a distance $\approx d$ from the walls, in the region of highest mean velocity gradient: this confirms their dependence on the local shear rate. These features are qualitatively similar to the measurements reported in Ref. [38] and to the numerical simulations presented in Ref. [18].

C. Transverse velocity fluctuations

As expected, the normalized average of the transverse velocity component is very small, $\overline{v_y}/\overline{V_x} \lesssim 3 \times 10^{-3}$. However, the instantaneous transverse velocity of individual particles v_y is not zero, due to their interactions. Like for the fluctuations of v_x , we characterize those of v_y by the average $\sigma_{V_y}(y)$ over early times of their root mean square $[v_y^2 - V_y^2(y, t)]^{1/2}$. This allows us to compare longitudinal and transverse velocity fluctuations measured simultaneously; this comparison had only been previously performed on numerical simulations [18]. Figure 5 shows profiles of $\sigma_{V_y}(y)$ normalized by $\overline{V_x}d/H$ for $\phi = 30\%$ and 40% . Like $\sigma_{V_x}(y)$, $\sigma_{V_y}(y)$ is smallest at the center of the gap and largest near the walls, and qualitatively follows the variation of the local shear rate. Moreover, the maximum value of $\sigma_{V_y}(y)$ is higher for the largest particle volume fraction $\phi = 40\%$ while the minimum near the center of the gap is broader. These features reflect variations of the local shear rate due to the more blunted velocity profile at $\phi = 40\%$. Compared with the longitudinal velocity fluctuations, the maximum of the transverse fluctuations takes place at a larger distance from the wall and its amplitude is lower. These results are in reasonable agreement with those reported in Ref. [18]. In contrast, transverse velocity fluctuations larger than longitudinal velocity fluctuations were reported for numerical simulations in an unbounded simple shear flow [13]. However, the

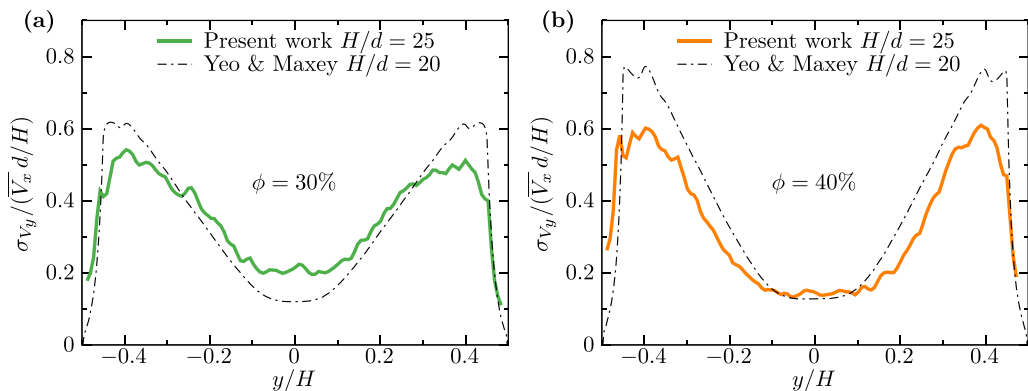


FIG. 5. Normalized rms of the transverse velocity across the gap compared with numerical results from Ref. [18]. Same experiments as in Fig. 3.

lack of side walls and the uniform shear in the simulations do not allow for a meaningful direct comparison with our results.

D. Correlation of transverse and longitudinal velocity fluctuations

The correlation of the longitudinal and transverse velocities can be an indicator of irreversible behavior in the pair interaction of particles, with a negative value (given a positive velocity gradient) for sheared suspensions [13]. Like the individual fluctuations (σ_{v_x} , σ_{v_y}), this magnitude is also expected to grow linearly with the velocity gradient and the particle size, and to grow monotonically with the volume fraction.

For each tracked particle we compute $\delta v_x \delta v_y$ where $\delta v_x = v_x - V_x(y, t)$ and $\delta v_y = v_y$ are the components of its velocity fluctuations with respect to the instantaneous velocity profile $V_x(y, t)$ (we assume $V_y(y, t) \approx 0$ due to confinement). Afterwards, we follow a scheme similar to the one described in Sec. III A for averaging, first, along the length and then, in time. Since this correlation is expected to change sign with the flow reversal, we multiply by -1 the values for the second half of the oscillation, during backward motion of the suspension [$\overline{V_x(t)} < 0$]; otherwise, the contributions from each half-cycle cancel out.

Figure 6 shows the results of this calculation $\overline{\delta v_x \delta v_y}$ normalized by $(\overline{V_x} d/H)^2$. The correlation presents the expected trends: it has a sign opposite to the velocity gradient $\partial V_x / \partial y$, increases in

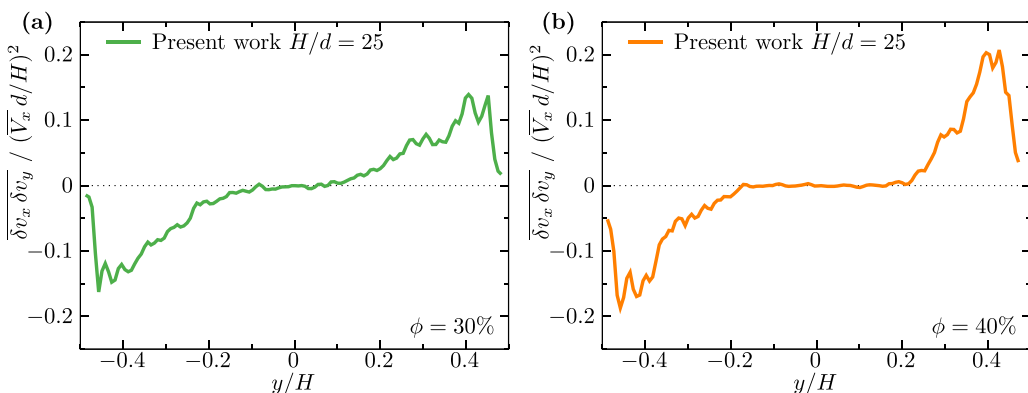


FIG. 6. Correlation of transverse and longitudinal velocity fluctuations. Same experiments as in Fig. 3.

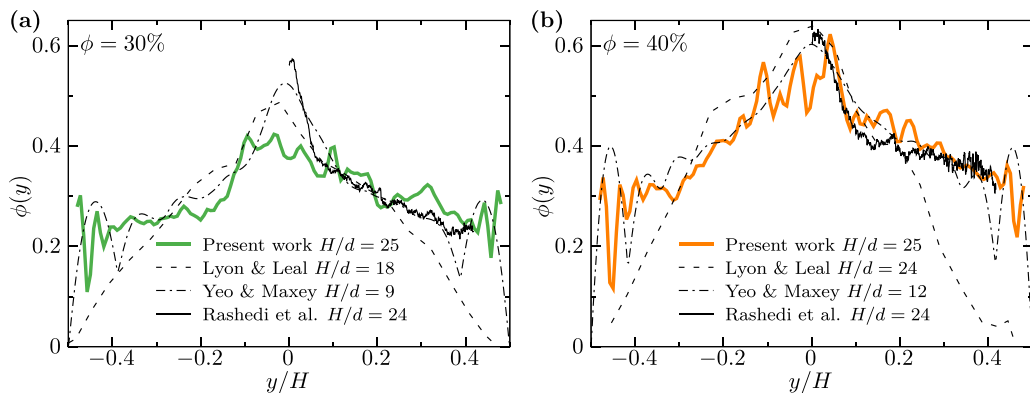


FIG. 7. Profile $\phi(y)$ across the gap of the local particle volume fraction estimated by counting of tagged particles in the initial flow state compared with experimental and numerical results from the literature.

magnitude with it (maximum near the walls, zero in the center) and increases with the volume fraction.

E. Particle volume fraction profiles

We estimate the local particle volume fraction $\phi(y)$ across the gap from the number $n(y)$ of dyed particles in a series of bins of equal width. Assuming that $n(y)$ is proportional to the local volume fraction, we have $\phi(y) \approx \phi n(y)/\bar{n}$, where ϕ is the mean volume fraction and \bar{n} is the average of $n(y)$ across y . The measured values of $\phi(y)$ present a significant dispersion due to the small fraction of dyed particles: we therefore average the profiles obtained for the same mean volume fraction ϕ from five different experiments (with oscillation amplitudes A_0/H between 4.6 and 11.6). In Fig. 7, the resulting profiles $\phi(y)$ are compared with experimental and numerical results from the literature [18,24,38].

In the central 20% of the gap ($-0.1 \leq y/H \leq 0.1$), the volume fractions $\phi(y)$ present a maximum which is higher and narrower for $\phi = 40\%$; in this case, the variation of $\phi(y)$ with y is similar to that reported by Yeo and Maxey [18] and Rashedi *et al.* [24]. These results are consistent with a shear-induced migration of the particles toward the gap center that takes place when the cell is filled by the suspension before each experiment.¹

IV. INSTABILITY AND TRANSVERSE FLOW

A. Influence of the instability on particle trajectories

Figure 8 shows the trajectory of an individual particle located in the center part of the gap during the development of the instability. It is clear that the amplitude of the oscillations of the position of the particle along the flow (coordinate x) remains of the same order of magnitude even as the instability develops. Note that this amplitude is more than 50 times larger than the corresponding variations of the coordinate y , in qualitative agreement with the magnitude of the

¹Previous experiments reported in Ref. [28] were performed in a similar setup using dyed fluorescent fluid and transparent particles. The observation of a bright band in the middle of the gap [Fig. 6(b) in Ref. [28]] suggested incorrectly a low particle volume fraction zone: this was due to a parasitic fluorescence eliminated in the present work. This bright band corresponded actually to the peak of particle volume fraction shown in Fig. 7. Note that this observation of a higher particle volume fraction in the center of the gap invalidates possible explanations of the instability that assume a larger fraction of particles near the walls [28].

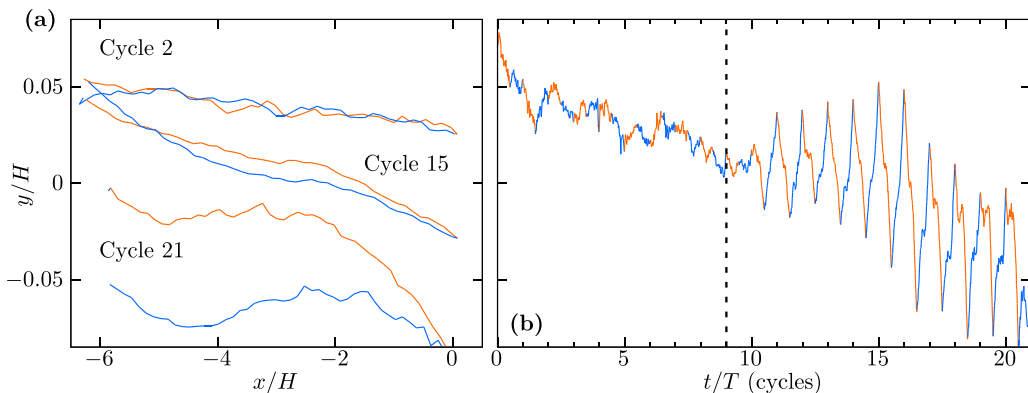


FIG. 8. (a) Trajectories in the (x, y) plane of one particle located in the center of the gap during three oscillation cycles in the initial state (cycle 2) and after (cycles 15 and 21) the onset of the instability. (b) Time variation of the transverse position y/H . Dashed vertical line: approximate onset of the instability. Orange shows forward flow ($\overline{V}_x(t) > 0$), blue shows reverse flow ($\overline{V}_x(t) < 0$). $\phi = 35\%$, $A_0/H = 4.6$.

velocity fluctuations presented in Fig. 5. Before the development of the instability, the transverse displacements are small and the particle follows roughly the same path in each half period [see cycle 2 in Fig. 8(a)] with a small global drift [see the evolution of the transverse position in time in Fig. 8(b)]. The development of the instability ($t/T \approx 9$) is marked by the emergence and growth of significantly larger transverse oscillations of the particle along y , with a period equal to that of the main flow. For this specific particle, Fig. 8(b) shows that, on average, $v_y > 0$ for $\overline{V}_x(t) < 0$ and $v_y < 0$ for $\overline{V}_x(t) > 0$, after the onset of the instability. However, the temporal variation of v_y differs from that of v_x as shown by the shape of cycles 15 and 21 and the increasing transverse separation between the two half cycles in Fig. 8(a).

B. Structure of the transverse velocity field

To obtain information on the variation of the transverse velocity along the cell length, we calculated the instantaneous profile $V_y^{\text{center}}(x, t)$ of its average in a central band ($-0.1 \leq y/H \leq 0.1$); this is analogous to the computation of longitudinal velocity profiles across the gap. The resulting normalized velocity $V_y^{\text{center}}(x, t)/\overline{V}_x$ is presented in a spatiotemporal diagram in Fig. 9. No clear periodic structure is visible before $t/T \approx 9$. At longer times, a “herringbone-like” pattern can be observed, in which V_y^{center} changes sign periodically (alternate blue and red colors in Fig. 9) both spatially (wavelength $\lambda/H \approx 3.5$) and in time (period T). The zigzag geometry of the pattern reflects the fact that the spatially periodic structure of the transversal velocity follows the longitudinal oscillations of the suspension.

To compute the time-averaged transverse velocity component along both the longitudinal and transverse directions, we used a reference frame following the longitudinal oscillation of the particles. The coordinate $x(t)$ of a given particle is replaced by the estimated material coordinate x_0 corresponding to its position at $t = 0$:

$$x_0 = x(t) - \int_0^t V_x(y(u), u) du. \quad (1)$$

At a given time, each detected particle is characterized by its coordinates x_0 and y and by its calculated velocity components v_x and v_y . Using the same binning procedure as before but in the (x_0, y) plane and averaging in time during half periods with the same direction of the main flow, we obtain the transverse velocity fields $V_y^+(x_0, y)$ and $V_y^-(x_0, y)$, corresponding to averages obtained during the forward [$\overline{V}_x(t) > 0$] and backward [$\overline{V}_x(t) < 0$] motion of the suspension, respectively.

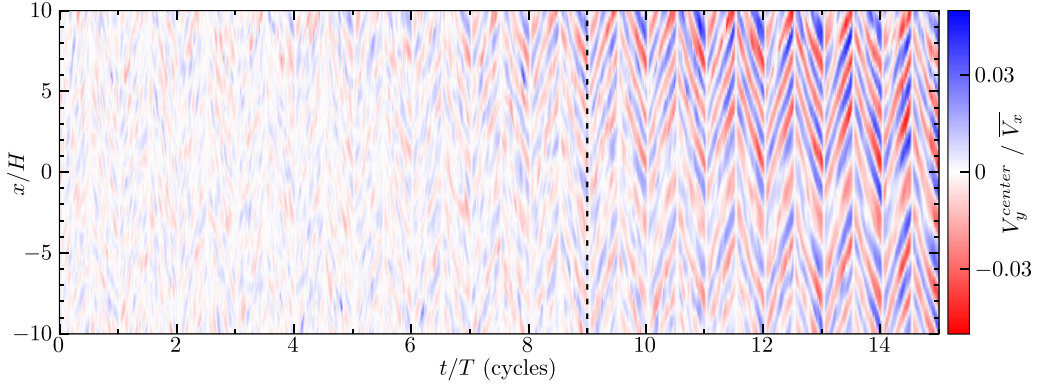


FIG. 9. Spatiotemporal diagram of the normalized transverse velocity $V_y^{\text{center}}/\bar{V}_x$ (color scale) as a function of t/T and x/H for $\phi = 35\%$ and $A_0/H = 4.6$ (same experiment as in Fig. 8). $t = 0$ corresponds to the beginning of the flow oscillation.

These averages are presented as color maps in Fig. 10. The upper ($y > 0$) and lower ($y < 0$) halves of the maps correspond to $V_y^+(x_0, y)/\bar{V}_x$ and $V_y^-(x_0, y)/\bar{V}_x$, respectively (both maps are symmetric with respect to $y = 0$). Note that the variations displayed in Fig. 10 correspond only to the contribution of the instability; that of the random velocity fluctuations is essentially eliminated by averaging over time.

During the first oscillation cycles [Fig. 10(a)], one observes only a disordered pattern of velocity variations in the maps, confirming that the particle velocity is parallel to the main flow, except for random fluctuations. After the instability has developed [Fig. 10(b)], both $V_y^+(x_0, y)$ and $V_y^-(x_0, y)$ vary periodically with x_0 . The magnitude of the transverse velocity is smaller near the walls, as shown by the lighter colors of the map in this region. The periodic variation along x_0 is present in both sets $V_y^+(x_0, y)$ and $V_y^-(x_0, y)$ but with opposite signs, as seen by comparing the two halves in Fig. 10(b).

To compare the present instability to that observed previously [28], we prepared a suspension of PMMA particles without matching the optical index of the liquid to make them visible; the same cell as before is now illuminated uniformly from behind the (x, z) plane of its width and length in

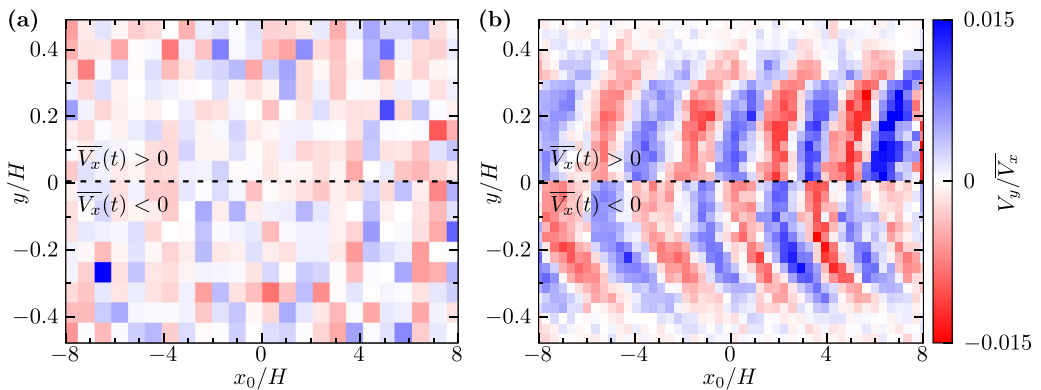


FIG. 10. Maps in the (x_0, y) plane of the normalized transverse velocities components (color scale) $V_y^+(x_0, y)/\bar{V}_x$ (upper half) and $V_y^-(x_0, y)/\bar{V}_x$ (lower half), averaged over two sets of half periods. (a) Average over the first four cycles of oscillation. (b) Average over 58 oscillations for which the instability is present (cycles 17–75). Same experiment as in Fig. 9 ($\phi = 35\%$, $A_0/H = 4.6$).

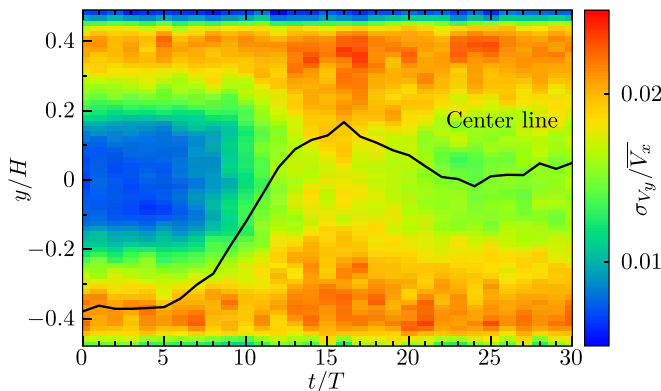


FIG. 11. Variation as a function of y and t of the normalized rms of the transverse velocity $\sigma_{V_y}/\overline{V_x}$ (color scale) for $\phi = 35\%$ and $A_0/H = 4.6$ (same experiment as in Fig. 9). Each column corresponds to the average over one cycle. Black curve shows time variation of the spatial average of $\sigma_{V_y}/\overline{V_x}$ over the interval $-0.1 < y/H < 0.1$ (same vertical axis as for the color scale).

order to map light transmission. Periodic stripes of the same type as those presented in Ref. [28] are observed for similar amplitudes and periods of the flow oscillations. In both cases, these structures follow the oscillations of the main flow and their wavelength is the same as that of the transverse velocity field shown above, within experimental uncertainty. This confirms that the results presented in the present work correspond to the same instability as that reported in Ref. [28].

V. DYNAMICS OF THE GROWTH OF THE INSTABILITY

A. Time dependence of the transverse velocity

The variation of the normalized rms of the transverse velocity fluctuations $\sigma_{V_y}(y, t)/\overline{V_x}$ with time and across the gap is presented in the spatiotemporal diagram of Fig. 11. We use σ_{V_y} instead of directly V_y which, as mentioned in Sec. IV B, has a very small average value along x . There is a sharp increase of $\sigma_{V_y}(y, t)/\overline{V_x}$ in the center of the gap ($-0.15 \lesssim y/H \lesssim 0.15$) for $t/T \approx 9$ as the instability develops, and a peak value is reached for $t/T \approx 15$ (black curve in Fig. 11). We note that the magnitude of $\sigma_{V_y}(y, t)/\overline{V_x}$ is initially ($t/T \lesssim 5$ in this experiment) small in this central region, as shown before in Fig. 5. In contrast, closer to the walls ($|y/H| \approx 0.4$), the magnitude of the fluctuations is larger and not significantly influenced by the development of the instability, as shown by the constant color shade: in this region, $\sigma_{V_y}(y, t)$ is mostly due to random velocity fluctuations.

Globally, $\sigma_{V_y}(y, t)$ includes the effect of both the periodic instability and the random velocity fluctuations; in addition, it does not provide information on the spatial periodicity of the transverse velocity. A more detailed characterization of the instability, that is also less affected by the random velocity fluctuations, is provided by the autocorrelation along the flow direction of the instantaneous transverse velocity $V_y^{\text{center}}(x, t)$ calculated in Sec. IV B,

$$F_{V_y}(\delta x, t) = \int V_y^{\text{center}}(x, t) V_y^{\text{center}}(x - \delta x, t) dx. \quad (2)$$

The spatiotemporal diagram of Fig. 12(a) shows alternate zones of positive and negative values of F_{V_y} (color scale) visible only after the instability has developed. The separation between two maxima of the autocorrelation corresponds to the normalized wavelength λ/H of the transverse velocity field (the black line in the figure marks the first maximum). The number and spacings of the bands are not exactly constant with time and rearrangements occur: in the figure, for instance,

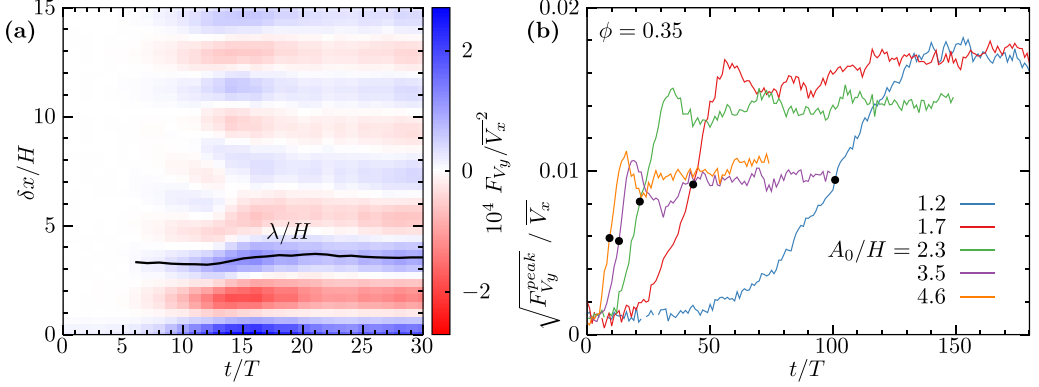


FIG. 12. (a) Spatiotemporal diagram of the normalized autocorrelation function $F_{V_y}(\delta x, t)/\overline{V_x^2}$ of V_y^{center} (color scale) versus $\delta x/H$ (vertical scale) and t/T (horizontal scale). Data are averaged over one cycle; values for $\delta x \leq 0$ are symmetrical to those for $\delta x \geq 0$. Same experiment as in Fig. 9 ($\phi = 35\%$, $A_0/H = 4.6$). Black line shows value of $\delta x/H = \lambda/H$ corresponding to first autocorrelation peak. (b) First autocorrelation peak amplitude as a function of t/T . Same parameters as in panel (a) (except for A_0/H). Black dots indicate time t_{50}/T , corresponding to half the maximum of the peak amplitude.

a band disappears at $\delta x/H \approx 6$ for $t/T \approx 13$. The dependence of λ/H on the period and amplitude of the oscillation and on the gap H is discussed in detail in Ref. [28].

Figure 12(b) shows the time evolution of the normalized magnitude of the first autocorrelation peak $[F_{V_y}^{\text{peak}}(t)]^{1/2}/\overline{V_x}$ for different values of the amplitude A_0/H of the flow oscillation. The curves start at a lower relative value (compared with their maximum) than, for example, the variation of $\sigma_{V_y}/\overline{V_x}$ in Fig. 11: this confirms the expectation of a smaller influence of the nonperiodic random velocity fluctuations on the autocorrelation peaks and of a response that is more specific to the instability. For all curves, the peak magnitude rises toward a first maximum and, then, drops slightly before becoming nearly constant. This maximum and the time at which it is reached vary significantly with A_0/H , as discussed below. The presence of such a maximum may reflect a redistribution of the particles in the gap induced by the transverse flow after the development of the instability.

The five curves in Fig. 12(b) correspond to experiments where $A_0 = V_0 T/2$ varies while keeping the same flow rate, so that the Reynolds number remains constant ($\text{Re} = 0.2$). We compare then, in Fig. 13, experiments corresponding to three different Reynolds numbers spanning four decades, $\text{Re} = 4 \times 10^{-5}$, 5×10^{-2} , and 0.4 , but within a narrow range of amplitudes ($3.6 \leq A_0/H \leq 4.6$). This was achieved by using fluids of different viscosities ($\mu_0 = 7.6 \text{ mPa s}$ and 3.2 Pa s) and different flow rates Q_0 . Variations of the autocorrelation peak with t/T are almost identical, suggesting that inertia does not influence the development of the instability at the low Reynolds numbers used here ($\text{Re} \leq 0.4$).

B. Characteristic growth rate

In the following, we characterize the growth rate of the instability by the time t_{50} at which the first autocorrelation peak reaches half its maximum amplitude. This point is marked by a black dot in the curves shown in Figs. 12(b) and 13. The corresponding growth rate is then $1/t_{50}$ and we will use T/t_{50} as its dimensionless form. Alternatively, the curves were fit with exponential functions before their increase levels off, but the values of the corresponding characteristic times were more dispersed.

Figure 14(a) shows the variation of T/t_{50} with the oscillation amplitude A_0/H for a constant gap H but different volume fractions. Figure 14(b) shows instead this same variation for two

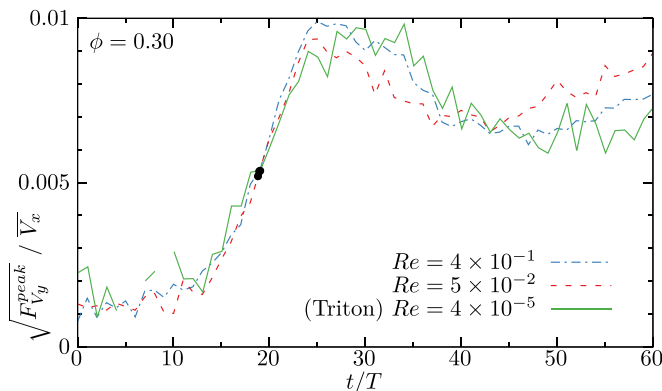


FIG. 13. Variations of the normalized first autocorrelation peak with t/T for three different Reynolds numbers over a range of four decades. Black dots indicate time t_{50}/T , corresponding to half the maximum value of the correlation peak amplitude.

different gaps H but the same volume fraction $\phi = 40\%$. In both Figs. 14(a) and 14(b), T/t_{50} varies approximately linearly with the amplitude A_0/H , with a threshold of the order of $A_0/H \simeq 1$ and a saturation at large amplitudes. The slopes obtained from a linear fit of the data increase with ϕ and decrease with H by a factor of four when H doubles (compatible with a variation as $1/H^2$).

We can therefore suggest the following dependence of the dimensionless growth rate:

$$\frac{T}{t_{50}} = f(\phi) \left[\frac{d}{H} \right]^2 \frac{A_0}{H}, \quad (3)$$

where $f(\phi)$ is a dimensionless function to be determined. Since $A_0/H = V_0 T / (2H)$, the growth rate satisfies

$$s_{50} = \frac{1}{t_{50}} = \frac{1}{6} f(\phi) \dot{\gamma} \left[\frac{d}{H} \right]^2, \quad (4)$$

where $\dot{\gamma} = 3V_0/H$ is the average shear rate for Poiseuille flow.

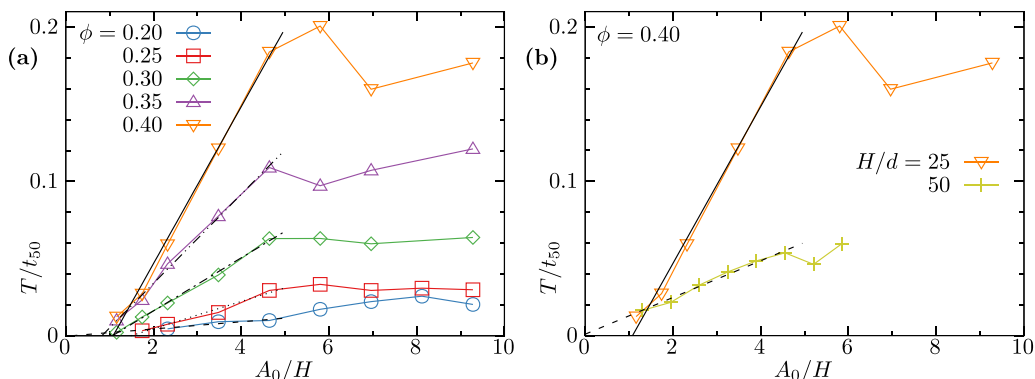


FIG. 14. Variation of the dimensionless growth rate T/t_{50} versus the normalized oscillation amplitude A_0/H for (a) $H = 1$ mm and $20\% \leq \phi \leq 40\%$ and (b) for $H = 1$ and 2 mm and $\phi = 40\%$. Straight lines show best linear fit to the data for $A_0/H \lesssim 5$.

VI. DISCUSSION OF THE RESULTS

We now seek to account for expression (4) of the characteristic time t_{50} . As shown above, the comparison of experiments at different Reynolds numbers demonstrates that inertia is not a relevant parameter. Therefore the characteristic timescale should be associated with the Shear-Induced Migration (SIM) of the particles.

For determining the characteristic time τ_{SIM} and the corresponding induction length L_{SIM} for achieving segregation by SIM, we estimate first the corresponding diffusion coefficient D_{SIM} by means of the relation from Ref. [15]:

$$D_{\text{SIM}}(\phi) = g(\phi) \dot{\gamma} (d/2)^2. \quad (5)$$

In the present geometry, the average shear rate $\dot{\gamma}$ is taken equal to the value $3V_0/H$ for Poiseuille flows and the dimensionless function $g(\phi)$ is given by [38,39]

$$g(\phi) = \frac{1}{3}\phi^2 \left(1 + \frac{1}{2}e^{8.8\phi} \right). \quad (6)$$

The characteristic time for diffusion across each half of the gap thickness is then [17]

$$\tau_{\text{SIM}} = (H/2)^2 / (4D_{\text{SIM}}). \quad (7)$$

Equation (7) allows us to estimate a dimensionless induction length parallel to the flow $L_{\text{SIM}}/H = V_0\tau_{\text{SIM}}/H$ which satisfies:

$$\frac{L_{\text{SIM}}}{H} = \frac{1}{12g(\phi)} \left(\frac{H}{d} \right)^2. \quad (8)$$

For the present experiments with $H = 1$ mm, $d = 40$ μm , and $\phi = 40\%$ gives $L_{\text{SIM}} \approx 55$ mm. Taking into account Eq. (6), it is clear that L_{SIM} is even larger for lower volume fractions. Therefore, the characteristic induction length is at least of the same order of magnitude as the typical distance from the cell inlet to the observed location (≈ 100 mm). This implies that large travel lengths may be necessary to reach equilibrium volume fraction profiles, particularly at low volume fractions. In the case of a steady flow in a very long channel, the experimental results from Ref. [24] give $L_{\text{SIM}}/H \approx 1000$ for $\phi = 40\%$, $H = 2$ mm, $d = 80$ μm .

We compare below the dimensionless growth rate T/τ_{50} of the instability to the corresponding ratio T/τ_{SIM} . Then, computing τ_{SIM} from Eq. (7) and using the relations: $\dot{\gamma} = 3V_0/H$ and $A_0 = V_0T/2$, one obtains the expression

$$\frac{T}{\tau_{\text{SIM}}} = 24g(\phi) \frac{A_0}{H} \left(\frac{d}{H} \right)^2. \quad (9)$$

The ratio of times T/τ_{SIM} is actually equal to the ratio of distances $2A_0/L_{\text{SIM}}$ and is always $\lesssim 0.2$ in the present experiments.

The equation above predicts a linear increase of T/τ_{SIM} with the normalized oscillation amplitude A_0/H , as observed in the experiments shown in Fig. 14. It also predicts a quadratic dependence on the particle size d . In Fig. 15(a), we plot $(T/t_{50})/[24g(\phi)(d/H)^2]$ as a function of A_0/H in order to check the validity of Eq. (9). All the experimental curves collapse indeed onto the same universal curve close to the diagonal A_0/H indicated by a dashed black line. However, several of the curves present a threshold for $A_0/H \approx 1$, as also observed in Fig. 14. This might be due to a transition from a reversible (no evolution of the system from period to period) to an irreversible oscillation regime [26,40].

To show the influence of the volume fraction ϕ on the growth rate, in Fig. 15(b) we plot the function $f(\phi)$ from Eq. (3), computed as the product of the slopes of the linear fits shown in Fig. 14 by $(H/d)^2$. The corresponding prefactor for T/τ_{SIM} is $24g(\phi)$: it is estimated by means of Eq. (6) and plotted for comparison in Fig. 15(b) as a dashed line. We observe a fast increase of both variables with ϕ and their similar values.

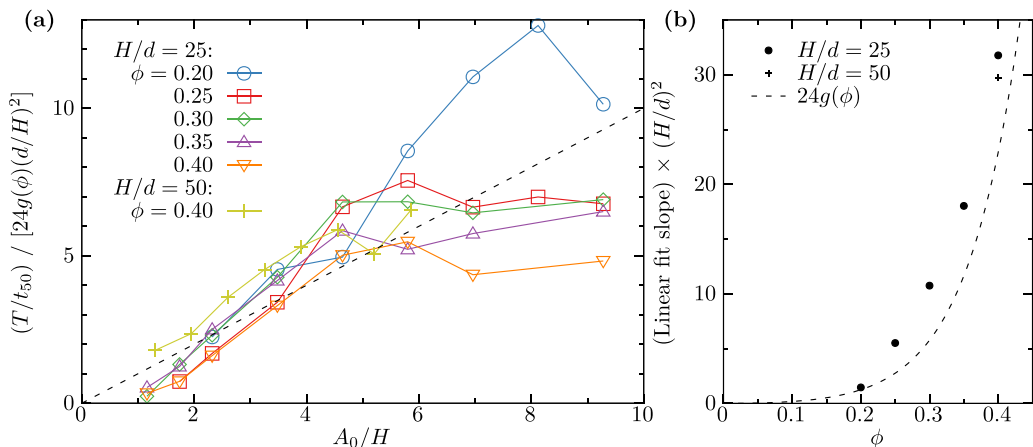


FIG. 15. (a) Plots of $(T/t_{50})/[24g(\phi)(d/H)^2]$ as a function of A_0/H for different volume fractions ϕ and gaps H/d . The dashed line of slope 1 is a plot of A_0/H . (b) Plot of the estimation of $f(\phi)$ from the data in panel (a) and of $24g(\phi)$ (dashed curve) versus ϕ .

The dimensionless growth rate T/t_{50} increases linearly with the normalized oscillation amplitude A_0/H for $A_0/H < 5$; for larger values of A_0/H the growth rate remains approximately constant. These observations suggest that the growth of the transverse velocities results from the repetition of a process taking place after each flow reversal and active up to a finite travel distance.

VII. CONCLUSION

We investigated the oscillatory flow of neutrally buoyant, non-Brownian suspensions in Hele-Shaw cells. Tracking a small fraction of all particles in a plane parallel to the main flow and the gap, we quantitatively determine particle velocity components parallel and transverse to the mean flow and estimate particle volume fraction profiles.

Results obtained in the initial state, before the instability appears, qualitatively agree with previous results for flow through narrow channels [24,38]. Following the initial injection of the suspension into the cell, we observe a shear-induced migration of particles towards the center and blunted velocity profiles. Moreover, the measured velocity fluctuations in both directions (longitudinal and transverse) are in good agreement with the numerical results from Ref. [18].

At longer times, the suspension develops an instability marked by the occurrence of a nonzero velocity transverse to the mean flow and perpendicular to the gap walls. This component is periodic both with time and distance along the mean flow, giving the instability the form of stripes transverse to the oscillation. This instability has been observed consistently for $20\% \leq \phi \leq 40\%$. The amplitude of this periodic structure, characterized by the first peak of the spatial autocorrelation of the transverse velocity, increases with time until it reaches a maximum value and, then, decreases slightly.

We estimate a growth rate from the inverse of the number of cycles before reaching half the maximum amplitude (T/t_{50}). This growth rate varies linearly with the oscillation amplitude A_0/H , with a threshold at $A_0/H \approx 1$ and a saturation at large oscillation amplitudes; the threshold may reflect a reversible motion of the particles at small amplitudes A_0/H . Focusing our attention on the linear region, we observe that the slopes increase with the volume fraction ϕ and decrease with the gap thickness H . Ruling out the influence of inertia, we show that a growth rate estimated from the shear-induced transport across the gap has a similar dependence on the volume fraction and the gap thickness as the measured T/t_{50} values.

Finally, this instability has not been observed in circular cylindrical tubes for analogous experimental conditions [19]. Therefore, the rectangular cross section of our cells might be required for observing the instability due to specific features in that geometry such as secondary flows [20,22]. This issue deserves further investigation.

ACKNOWLEDGMENTS

This work was funded by the research project UBACYT 20020170100225BA. One of us (A.A.G.) is supported by a doctoral fellowship from the University of Buenos Aires and by the ADI program of the Paris-Saclay University. Funding of exchange visits during the thesis has been provided by the CNRS-CONICET International Research Program IRP-IVMF (green engineering for fluid mechanics). We thank R. Pidoux, L. Auffray, and A. Aubertin for their help in the realization of the experimental setups and C. Manquest for suspension characterization.

-
- [1] J. F. Morris, Toward a fluid mechanics of suspensions, *Phys. Rev. Fluids* **5**, 110519 (2020).
 - [2] S. Gallier, E. Lemaire, F. Peters, and L. Lobry, Rheology of sheared suspensions of rough frictional particles, *J. Fluid Mech.* **757**, 514 (2014).
 - [3] A. Singh, R. Mari, M. M. Denn, and J. F. Morris, A constitutive model for simple shear of dense frictional suspensions, *J. Rheol. (Melville, NY, US)* **62**, 457 (2018).
 - [4] F. Peters, G. Ghigliotti, S. Gallier, F. Blanc, E. Lemaire, and L. Lobry, Rheology of non-Brownian suspensions of rough frictional particles under shear reversal: A numerical study, *J. Rheol. (Melville, NY, US)* **60**, 715 (2016).
 - [5] J. F. Morris and F. Boulay, Curvilinear flows of noncolloidal suspensions: The role of normal stresses, *J. Rheol. (Melville, NY, US)* **43**, 1213 (1999).
 - [6] A. Deboeuf, G. Gauthier, J. Martin, Y. Yurkovetsky, and J. F. Morris, Particle Pressure in a Sheared Suspension: A Bridge from Osmosis to Granular Dilatancy, *Phys. Rev. Lett.* **102**, 108301 (2009).
 - [7] F. Boyer, E. Guazzelli, and O. Pouliquen, Unifying Suspension and Granular Rheology, *Phys. Rev. Lett.* **107**, 188301 (2011).
 - [8] S. Garland, G. Gauthier, J. Martin, and J. Morris, Normal stress measurements in sheared non-Brownian suspensions, *J. Rheol. (Melville, NY, US)* **57**, 71 (2013).
 - [9] I. E. Zarraga, D. A. Hill, and D. T. Leighton Jr., The characterization of the total stress of concentrated suspensions of noncolloidal spheres in newtonian fluids, *J. Rheol. (Melville, NY, US)* **44**, 185 (2000).
 - [10] É. Couturier, F. Boyer, O. Pouliquen, and É. Guazzelli, Suspensions in a tilted trough: Second normal stress difference, *J. Fluid Mech.* **686**, 26 (2011).
 - [11] F. Da Cunha and E. Hinch, Shear-induced dispersion in a dilute suspension of rough spheres, *J. Fluid Mech.* **309**, 211 (1996).
 - [12] G. Drazer, J. Koplik, B. Khusid, and A. Acrivos, Deterministic and stochastic behaviour of non-Brownian spheres in sheared suspensions, *J. Fluid Mech.* **460**, 307 (2002).
 - [13] G. Drazer, J. Koplik, B. Khusid, and A. Acrivos, Microstructure and velocity fluctuations in sheared suspensions, *J. Fluid Mech.* **511**, 237 (2004).
 - [14] J. Martin, N. Rakotomalala, and D. Salin, Hydrodynamic Dispersion of Noncolloidal Suspensions: Measurement from Einstein's Argument, *Phys. Rev. Lett.* **74**, 1347 (1995).
 - [15] D. Leighton and A. Acrivos, The shear-induced migration of particles in concentrated suspensions, *J. Fluid Mech.* **181**, 415 (1987).
 - [16] R. J. Phillips, R. C. Armstrong, R. A. Brown, A. L. Graham, and J. R. Abbott, A constitutive equation for concentrated suspensions that accounts for shear-induced particle migration, *Phys. Fluids A* **4**, 30 (1992).
 - [17] P. R. Nott and J. F. Brady, Pressure-driven flow of suspensions: Simulation and theory, *J. Fluid Mech.* **275**, 157 (1994).
 - [18] K. Yeo and M. R. Maxey, Numerical simulations of concentrated suspensions of monodisperse particles in a poiseuille flow, *J. Fluid Mech.* **682**, 491 (2011).

- [19] B. Snook, J. E. Butler, and E. Guazzelli, Dynamics of shear-induced migration of spherical particles in oscillatory pipe flow, *J. Fluid Mech.* **786**, 128 (2016).
- [20] A. Ramachandran and D. T. Leighton, The influence of secondary flows induced by normal stress differences on the shear-induced migration of particles in concentrated suspensions, *J. Fluid Mech.* **603**, 207 (2008).
- [21] A. Ramachandran, Secondary convection due to second normal stress differences: A new mechanism for the mass transport of solutes in pressure-driven flows of concentrated, non-colloidal suspensions, *Soft Matter* **9**, 6824 (2013).
- [22] A. Zrehen and A. Ramachandran, Demonstration of Secondary Currents in the Pressure-Driven Flow of a Concentrated Suspension Through a Square Conduit, *Phys. Rev. Lett.* **110**, 018306 (2013).
- [23] S. Chakraborty and A. Ramachandran, A macrotransport equation for the Hele-Shaw flow of a concentrated suspension, *J. Fluid Mech.* **924**, A1 (2021).
- [24] A. Rashedi, M. Sarabian, M. Firouznia, D. Roberts, G. Ovarlez, and S. Hormozi, Shear-induced migration and axial development of particles in channel flows of non-Brownian suspensions, *AIChE J.* **66**, e17100 (2020).
- [25] F. Blanc, F. Peters, and E. Lemaire, Local transient rheological behavior of concentrated suspensions, *J. Rheol. (Melville, NY, US)* **55**, 835 (2011).
- [26] D. J. Pine, J. P. Gollub, J. F. Brady, and A. M. Leshansky, Chaos and threshold for irreversibility in sheared suspensions, *Nature (London)* **438**, 997 (2005).
- [27] L. Corte, P. M. Chaikin, J. P. Gollub, and D. J. Pine, Random organization in periodically driven systems, *Nat. Phys.* **4**, 420 (2008).
- [28] Y. L. Roht, I. Ippolito, J. P. Hulin, D. Salin, and G. Gauthier, Stripes instability of an oscillating non-Brownian iso-dense suspension of spheres, *Europhys. Lett.* **121**, 54002 (2018).
- [29] I. C. Carpen and J. F. Brady, Gravitational instability in suspension flow, *J. Fluid Mech.* **472**, 201 (2002).
- [30] D. J. Dhas and A. Roy, Stability of gravity-driven particle-laden flows—roles of shear-induced migration and normal stresses, *J. Fluid Mech.* **938**, A29 (2022).
- [31] J. F. Morris, A particularly unstable film, *J. Fluid Mech.* **944**, F1 (2022).
- [32] R. Moosavi, M. Maleki, M. R. Shaebani, J. C. Ruiz-Suárez, and E. Clément, Stripe formation in horizontally oscillating granular suspensions, *Europhys. Lett.* **107**, 34006 (2014).
- [33] G. Ovarlez, A. Vu Nguyen Le, W. J. Smit, A. Fall, R. Mari, G. Chatté, and A. Colin, Density waves in shear-thickening suspensions, *Sci. Adv.* **6**, eaay5589 (2020).
- [34] B. C. Bailey and M. Yoda, An aqueous low-viscosity density- and refractive index-matched suspension system, *Exp. Fluids* **35**, 1 (2003).
- [35] D. Borrero-Echeverry and B. C. A. Morrison, Aqueous ammonium thiocyanate solutions as refractive index-matching fluids with low density and viscosity, *Exp. Fluids* **57**, 123 (2016).
- [36] M. Lenoble, P. Snabre, and B. Pouligny, The flow of a very concentrated slurry in a parallel-plate device: Influence of gravity, *Phys. Fluids* **17**, 073303 (2005).
- [37] M. Souzy, P. Pham, and B. Metzger, Taylor’s experiment in a periodically sheared particulate suspension, *Phys. Rev. Fluids* **1**, 042001(R) (2016).
- [38] M. K. Lyon and L. G. Leal, An experimental study of the motion of concentrated suspensions in two-dimensional channel flow. Part 1. Monodisperse systems, *J. Fluid Mech.* **363**, 25 (1998).
- [39] D. Leighton and A. Acrivos, Viscous resuspension, *Chem. Eng. Sci.* **41**, 1377 (1986).
- [40] J. S. Guasto, A. S. Ross, and J. P. Gollub, Hydrodynamic irreversibility in particle suspensions with nonuniform strain, *Phys. Rev. E* **81**, 061401 (2010).